3D Phase-Field Simulation of Micropore Formation during Solidification: Morphological Analysis

H. Meidani[1], A. Jacot[1,2] and M. Rappaz[1]

[1] Computational Materials Laboratory, Institute of Materials, EPFL, Lausanne, Switzerland
[2] Calcom ESI SA, Parc Scientifique, PSE-A, Lausanne, Switzerland

E-mail: hossein.meidani@epfl.ch, michel.rappaz@epfl.ch

Abstract. A 3D multiphase-field (PhF) model has been developed in order to study the formation of a micropore constrained to grow in a solid network (i.e., pinching effect). The model accounts for the pressure difference due to capillarity between liquid and gas, the equilibrium condition at triple (solid-liquid-pore) lines, the partitioning and diffusion of dissolved gases such as hydrogen. From the predicted 3D morphology of the pore, entities such as the Interfacial Shape Distribution (ISD) are plotted and analyzed. It is shown that the mean curvature of the pore-liquid surface, and thus also the pressure inside the pore, is uniform. Despite the complex morphology of pores reconstructed using high-resolution X-ray tomography, the present PhF results suggest that a simple pinching model based on a spherical tip growing in between remaining liquid channels is a fairly good approximation.

1. Introduction

In order to better characterize and more importantly minimize the formation of micropores during the solidification of metals, a considerable effort has been dedicated to the modeling of pore formation [1]. These models, which range from very simple criteria functions [2] to sophisticated computational solutions of conservation and state equations, provide quantitative information on the effect of the processing conditions and alloy chemistry on microporosity [3–6]; including the effect of solidification shrinkage and gas segregation in the mushy zone.

Common to most advanced models of microporosity formation at the process scale is the consideration of average conservation equations. To close the problem mathematically, a constitutive model for the radius of the curvature of the pore as a function of its volume is required [5, 7–9]. If the pore is assumed to be spherical, this relationship is straightforward. However, in reality the growth of micropores is limited by the well-developed solid network. Due to numerous contacts with the solid phase, pores take a complex and highly tortuous shape. Local mean curvatures as high as $0.2\,\mu m^{-1}$ have been measured recently in aluminum alloys by X-ray tomography [10], i.e., the pressure difference between the pore and the surrounding liquid can be as high as 400 kPa. Since the pore is a compressible phase, this can substantially affect the pore size and fraction. For such situations, a so-called pinching model, i.e., a mathematical expression relating the radius of curvature of the pore-liquid interface, r_p, to the volume fraction of solid g_s, microstructural parameters and possibly the volume fraction of pores, g_p, is required. Different pinching models have been proposed. Initial models [8] assumed a spherical pore with a radius equal to half the dendritic arms spacing, $\lambda_2/2$. A more elaborate model of Pequet et al. [5] considers different stages: (i) the nucleated pore *escapes* its foreign substrate with a constant

radius; (ii) the pore is a growing sphere, (iii) it is pinched by the solid and its radius is given by a function of g_s and λ_2; (iv) the radius remains constant when interdendritic eutectic forms near the end of solidification. Poirier et al. [7] assumed the pores to be constrained by dendritic arms arranged in a hexagonal network, and introduced the effect of arms impingement into their model. Couturier and Rappaz [9] refined this model by assuming the pore to grow in between a regular arrangement of spherical grains (in 3D) or cylindrical dendrite arms (in 2D). The pores grow with an initial spherical shape until they come into contact with the solid phase: their radius of curvature is then assumed to be given by the largest sphere (3D) or cylinder (2D) that can fit in between the grains, respectively. In other words, they do not change their topology and are never forced to grow in between the solid.

A common point between these models is the simplified pore geometry. However, in reality, the pores have a much more complex shape. A phase-field (PhF) model, directly describing the pore morphology as a function of different parameters such as gas concentration, solid fraction and capillary forces was presented in [11], in 2D, and recently in 3D [12]. In the present contribution, the model is used to reproduce the pinching effect in 3D and study the morphology of a pore spanning over a distance larger than the dendritic arm spacing.

2. Model

A multiphase-field model is used in this study, for which a more detailed description can be found in [11, 12]. Three phase-field variables, $\phi_i(\mathbf{x}, t)$, where $i = s, l, p$ is a phase index, are introduced to show the distribution of the solid, liquid and pore, respectively, in time and space. These variables can be understood as local volume fractions and thus linked together using the constraint $\phi_s + \phi_l + \phi_g = 1$. One salient feature of the PhF method is a smooth and continuous variation of ϕ_i across any interface [13]. Spatial and temporal evolution of the phase-field variable ϕ_i is given by the following partial differential equation:

$$\dot{\phi}_i = \sum_{k \neq i} M_{ik} \begin{pmatrix} \epsilon_{ik}^2(\phi_k \nabla^2 \phi_i - \phi_i \nabla^2 \phi_k) \\ -2W_{ik}\phi_k^2(1-\phi_k)^2\phi_i(1-\phi_i)(1-2\phi_i) \\ -30\phi_i\phi_k(1-\phi_i)(1-\phi_k)\Delta G_{ik} - \Lambda \end{pmatrix} \tag{1}$$

with

$$\Delta G_{sl} = \Delta s_f \Delta T \quad \Delta G_{lp} = p_p - p_l \quad \Delta G_{sp} = 0 \tag{2}$$

and

$$W_{ik} = \frac{15\sqrt{2}\gamma_{ik}}{\delta_{ik}} \quad \epsilon_{ik}^2 = 2W_{ik}\delta_{ik}^2 \quad M_{ik} = \frac{\mu_{ik}}{\delta ik} \tag{3}$$

Here, Δs_f is the volumetric entropy of melting, ΔT is the undercooling, p_p and p_l are the pressures in the pore and liquid, respectively; ϵ_{ik}^2, M_{ik} and W_{ik} are the three PhF parameters associated with the physical parameters γ_{ik}, M_{ik} and W_{ik} describing the interfacial energy, the mobility and the interface thickness, respectively, between phases i and k [13]. The effect of the radius of curvature of the pore is taken into account through the driving force term for the liquid/pore transformation. It is expressed here as the pressure difference between the pore and liquid, which can be justified by solving the steady-state form of Eq. 1 in spherical coordinates, for a single pore surrounded by liquid. By doing so, the Laplace pressure condition is recovered:

$$p_p - p_l = 2\gamma_{lp}H \tag{4}$$

where H is the mean curvature of the pore. For a spherical pore of radius r_p, $H = r_p^{-1}$. Throughout this article, for the sake of simplicity, we will focus on aluminum alloys, where hydrogen is known to be the gas responsible of pore formation [10]. However, the model is more

general and can be applied to any alloy system in which a compressible phase forms.
The equilibrium solubility of hydrogen in the solid, c_s^H, and liquid, c_l^H, can be expressed as a function of p_p using Sievert's law, while assuming thermodynamical equilibrium at the interface:

$$c_s^H = S_s\sqrt{\frac{p_p}{p_0}} \quad c_l^H = S_l\sqrt{\frac{p_p}{p_0}} \tag{5}$$

where S_s and S_l are Sievert's constants (in $mole_H m^{-3}$) for the solid and liquid, respectively, and p_0 is the standard pressure. Taking local volumetric molar concentration of hydrogen and introducing Eq. 5 and the perfect gas law gives:

$$< c^H >= (\phi_s S_s + \phi_l S_l)\sqrt{\frac{p_p}{p_0}} + \phi_p \frac{2p_p}{RT} \tag{6}$$

The factor 2 in the last term is coming from the fact that hydrogen is in the form of H_2 in the pore.
Based on the experimental observations of Lee at al. [3, 4], finite rate hydrogen diffusion in the liquid is assumed to govern the growth kinetics of the pore. This has been taken into account in the model through a hydrogen conservation equation, neglecting any hydrogen concentration gradient in the gas phase and any hydrogen transport in the liquid due to convection:

$$\frac{\partial < c^H >}{\partial t} = \nabla \cdot (\phi_s D_s^H \nabla c_s^H + \phi_l D_l^H \nabla c_l^H) \tag{7}$$

A finite volume method with an explicit time-discretization scheme is used to numerically solve Eqs 1 and 7. At each time-step, the phase distribution is calculated by solving Eq. 1 and then, Eq. 7 is solved to calculate the concentration field. Besides, the calculation of the driving force terms of Eq. 1 requires solving the second order polynomial expression of Eq. 6 to obtain p_p from $< c^H >$. Since homogenization of the hydrogen concentration inside the pore is assumed to be infinitely fast (uniform pressure p_p), c^H is homogenized at each time-step inside the pore. For the diffusion and phase equations, no flux boundary condition is used. Therefore, the number of moles of hydrogen remains constant in the domain. Besides, due to the high computational cost of the 3D PhF calculations, the simulation domain is much smaller than the volume associated with one pore, i.e. n_p^{-1}, where n_p in the pore number density. Calculations were therefore undertaken at relatively large hydrogen contents (or supersaturation) in order to compensate for this effect.
As the model has already been presented in [11] and [12], the reader is referred to these publications for a more detailed description.

3. Analysis of pore curvature

Characterization of the pore-liquid interface in 3D requires computing its curvature in order to better understand the pinching effect. It is recalled that, for any surface patch, two principal radii of curvature, r_{p1} and r_{p2}, can be defined, from which two principal curvatures, $\kappa_1 = r_{p1}^{-1}$ and $\kappa_2 = r_{p2}^{-1}$, can be obtained. The local mean curvature, H, is then given by:

$$H = \frac{\kappa_1 + \kappa_2}{2} \tag{8}$$

For the problem at hand, only the pore-liquid interface is studied, using a similar method as in [12]. The iso-surface of the pore-liquid interface corresponding to $\phi_p = \phi_l = 0.5$ (i.e., $\phi_s = 0$) was extracted from the three-dimensional reconstruction of the results. Then, it

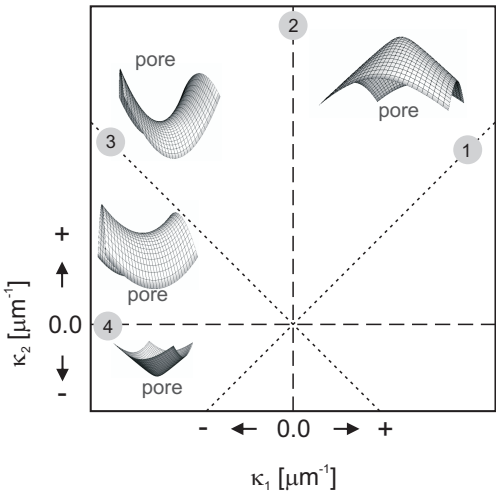

Figure 1. $\kappa_1 - \kappa_2$ space used to draw the Interfacial Shape Distribution (ISD) plot $P(\kappa_1, \kappa_2)$, representing the probability of having a surface element of the pore interface with the curvature (κ_1, κ_2). The curvature is measured with a unit surface normal pointing out of the pore.

was smoothened by triangular elements using the Avizo software (Avizo is a registered trade mark of Mercury Computer Systems, Chelmsford, Massachusetts). For each of the triangles composing this surface, which have a size close to the computational mesh, a quadratic surface was then best fitted considering a certain number (n_n) of triangular neighbors. Since curvature corresponds to first-derivatives of the unit surface normal along principal curvature directions [14], or second-derivatives of the surface positions, using nearest-neighbor triangles alone is not accurate enough. On the other hand, large values of n_n increase the calculation time and also result in a loss of accuracy by excessive smoothing of the surface. The best tradeoff between accuracy and performance was achieved with $n_n = 18$, while analyzing the curvature of a reference sphere.

For such 3D situations, a useful tool for a detailed analysis of the pore morphology based on both κ_1 and κ_2 is the Interfacial Shape Distribution (ISD) plot, first introduced by the group of Voorhees and coworkers for the analysis of coarsening of dendritic structures [15]. The ISD is a two-dimensional probability contour plot, $P(\kappa_1, \kappa_2)$, which measures the probability of having a surface patch, i.e., a triangular element in this case, with its principal curvatures falling in the range $[\kappa_1 - \Delta\kappa/2, \kappa_1 + \Delta\kappa/2]$ and $[\kappa_2 - \Delta\kappa/2, \kappa_2 + \Delta\kappa/2]$. Note that the areas of the triangular elements at which the curvature are estimated are taken into account in the statistics. The distribution $P(\kappa_1, \kappa_2)$ is then plotted in a (κ_1, κ_2) diagram in the form of isovalues. By definition, the curvatures are selected such that $\kappa_2 \geq \kappa_1$, therefore the distribution can have non-zero values only above the line $\kappa_2 = \kappa_1$, for which several regions can be distinguished in figure 1. They are separated by various lines : (1) Points on the line $\kappa_2 = \kappa_1$ correspond to pore-liquid surface elements having locally a spherical topology which can be convex ($H > 0$) or concave ($H < 0$); (2) Points along the line $\kappa_1 = 0$ ($\kappa_2 > 0$) correspond to pore elements with a convex cylindrical topology; (3) Along the line $\kappa_2 = -\kappa_1$, the pore surface has a saddle shape with a zero mean curvature; (4) Along the line $\kappa_2 = 0$ ($\kappa_1 < 0$), the pore surface element has also a cylindrical topology, but concave. In between these lines, a few morphologies have been illustrated.

4. Results and discussion

After being validated, in a similar manner as in [12], the model was used to study the morphology of a pore, pinched by a simplified solid network. Conceptually, the present porosity model can be applied to any complex geometrical situation such as a Representative Volume Element (RVE) obtained from X-ray micro-tomography [10]. However, because of the heavy computation time inherent to the PhF method and also because it is interesting to compare the present results

with analytical models of pinching [9], a simple situation is first considered here.
A simplified solid morphology, similar to the 3D model of Couturier et al. [9], was selected: it is composed of spherical solid grains arranged in the corners of a cubic network (which is referred to as *cubic RVE* throughout this article). In order to study the growth of a pore extending to distances larger than the dendritic arms spacing, a larger domain composed of two cubic RVEs was used (figure 2). An edge size of $\lambda_2 = 10\,\mu m$ was chosen, which is in fact the distance between two adjacent spherical grains. During the calculations, the radius of the solid grains is kept constant ($r_s = 5\,\mu m$), i.e. the evolution of the solid is neglected. Other parameters of the model are listed in Table 1.

Table 1. PhF model parameters

Parameter	Unit	Value
Mesh size (ΔX)	m	5.0×10^{-8}
δ_{ik}	m	1.2×10^{-8}
p_l	Pa	10^5
T	K	1000.0
M_{ls}	$m^3 J^{-1} s^{-1}$	1.0×10^{-6}
D_l	$m^2 s^{-1}$	1.0×10^{-6}
S_l	$mol_H m^{-3}$	0.7
S_s	$mol_H m^{-3}$	0.04
γ_{pl}	Jm^{-3}	0.9
γ_{ps}	Jm^{-3}	1.05
γ_{ls}	Jm^{-3}	0.15

A small spherical pore was nucleated at the center of the left octahedral space. Since the liquid is supersaturated in hydrogen, the pore grows. For a given initial hydrogen concentration c_0^H, the pore grows until equilibrium is reached, i.e., until the hydrogen content in the liquid is uniform and corresponds to the solubility limit of the final pressure p_p within the pore (Eq. 5). Initially, c_0^H was set to $7\,mol_H m^{-3}$ for which the final shape is spherical (figure 2.a). In order to obtain pores of different sizes, the hydrogen concentration was increased step-by-step, letting each time the pore to stabilize based on the new concentration. Morphologies of the pore at three instants corresponding to $c_0^H = 7, 24.3$ and $77.7\,mol_H m^{-3}$ are presented in figure 2. The different color patches in this figure indicate the local mean curvature. Areas with negative mean curvature (blue patches) are in contact with the solid and thus are characterized by a mean curvature $H_{ps} = -r_s^{-1} = -0.2\,\mu m^{-1}$. The main area of interest is the pore-liquid interface where the mean curvature is positive (red patches). This positive curvature is linked to the pressure difference between the pore and the liquid through the Laplace-Young equation (Eq. 4). Since p_p and p_l are homogenous, the mean curvature of the pore-liquid interface is also expected to be constant, which is the case here as shown by the uniform red color. The measured mean curvature for the pore-liquid interface shown in figure 2.a, b and c are $H = 0.505$, 0.276 and $0.282\,\mu m^{-1}$. These values are in good agreement with that obtained from the pressure difference $(p_p - p_l)$ extracted from the PhF calculations and Eq. 4 which give $H = 0.511$, 0.279 and $0.284\,\mu m^{-1}$, respectively. Each time that the pore was stabilized its radius of curvature at the pore-liquid interface, H^{-1}, was calculated using $(p_p - p_l)$ values extracted from the PhF calculations for various c_0^H values (figure 3). Considering physically the growth of a pore for a fixed value of r_s and λ_2 (and thus g_s), the maximum possible radius of a spherical pore is given by the model of Couturier, i.e., $r_p^{max} = \frac{\lambda_2\sqrt{3}}{2} - r_s$ (the conversion of r_s into g_s is straightforward up to $r_s = \lambda_2/\sqrt{2}$ and requires a few geometrical calculations above this limit, when the solid grains impinge on

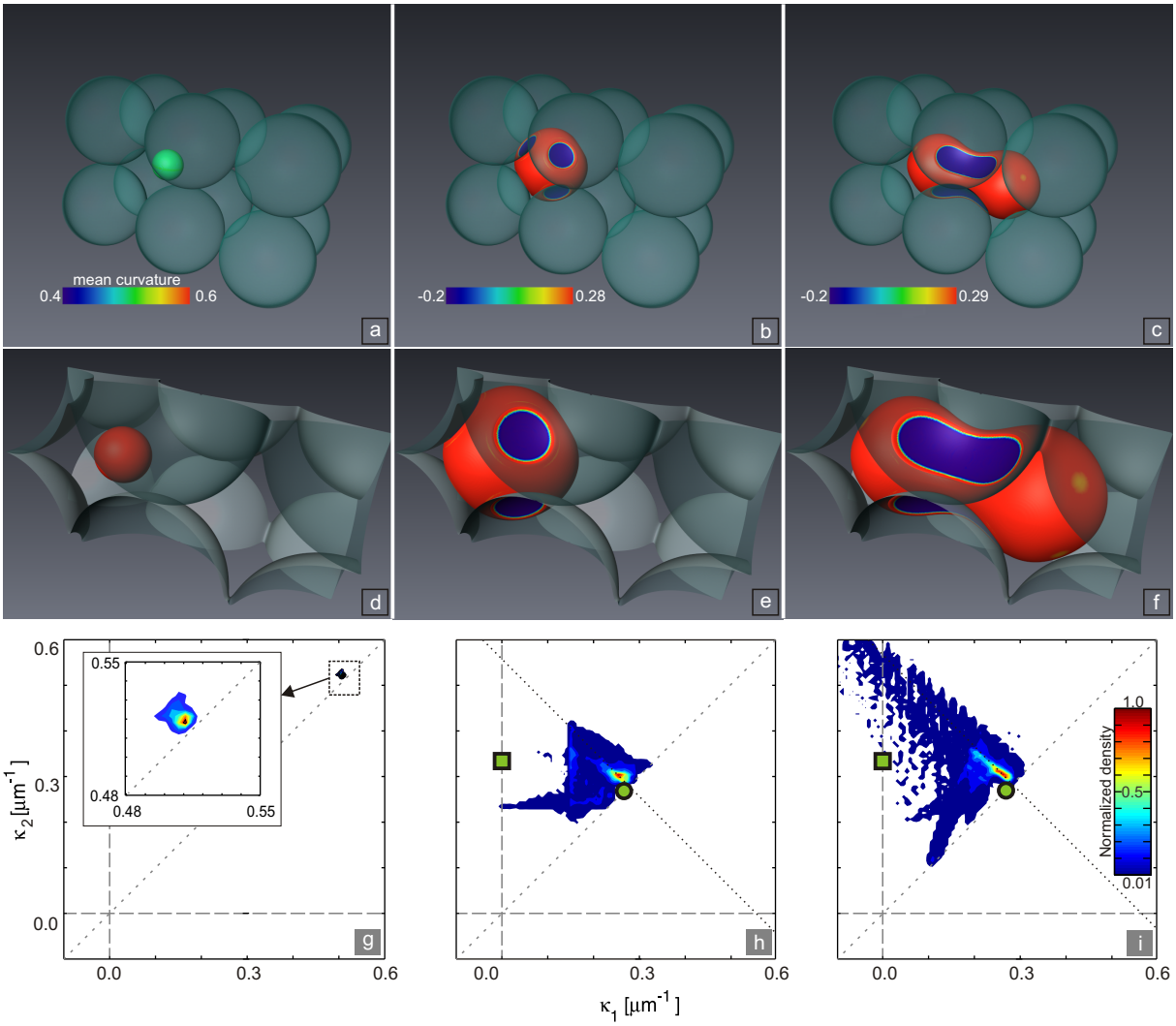

Figure 2. The morphology of pores, grown at $g_s = 0.53$ and for $c_0^H = 7$, 24.3 and 77.7$mol_H m^{-3}$ are presented in (a), (b) and (c), respectively, and with a higher magnification in (d), (e) and (f). The color of the pore shows the local mean curvature, calculated on the surface patches. The solid grains in contact with the pore are indicated by transparent spheres (cadet blue). The ISD plots corresponding to each pore are presented in (g), (h) and (i), taking into account the pore-liquid interface only. The green square and circle indicate the curvature given by the 2D and 3D model of Couturier [9], respectively.

each other [9, 12]). On the other hand, for a given value of r_s and λ_2, a minimum radius of curvature, r_p^{min} can also be defined: it corresponds to the radius of the curvature of a pore passing through the solid spheres in any face of the cubic RVE which is equal to the radius of a sphere that can be inscribed in between these solid spheres. It is thus given by $r_p^{min} = \frac{\lambda_2}{\sqrt{2}} - r_s$ up to $g_s = 0.965$. These maximum and minimum values are also presented in figure 3 with solid and dashed horizontal lines, respectively. The initial spherical pore has a radius of curvature even smaller than r_p^{min} (point **a** in figure 3). With an increase of c_0^H, it grows and comes into contact with the solid, at this point its radius is equal to r_p^{max}. Afterwards, with a further increase of c_0^H, the pore is pushed into the liquid channels with a decreasing H^{-1} (point **b** in

figure 3). Continuing to increase c_0^H, the pore is pushed more into the liquid channels until it can pass through one of the 6 openings on the faces of the cubic RVE. Here, the channel in the middle of the domain has been made 1% wider than the other ones, therefore the pore can pass through it before reaching the other faces of the RVE. While passing this channel, H^{-1} falls to its minimum given by the r_p^{min} line. After this, H^{-1} starts increasing again until it reaches the following layer of solid grains ahead of it (point **c** in figure 3). As already observed in a previous contribution for 2D cases [11], H^{-1} is also bound in 3D between two limits that are dictated by the solid morphology, namely the liquid channel widths. Considering a distribution of liquid channel widths in a casting, it sounds reasonable to define a mean value $r_p^{mean} = (r_p^{min} + r_p^{max})/2$ for the pinching effect that could be used in macroscopic porosity models.

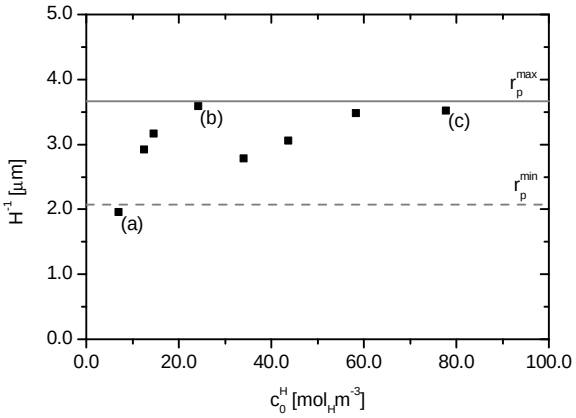

Figure 3. Radius of the curvature of the pore given by, H^{-1} for different c_0^H values calculated with the PhF model. The maximum and minimum possible values, r_p^{max} and r_p^{min}, are shown with the horizontal solid and dashed lines respectively. Points labeled (**a**), (**b**) and (**c**) correspond to 2

ISD plots corresponding to the pores presented in figure 2.a , b and c are plotted in the same figure in (g), (h) and (i), taking into account the pore interface in contact with the liquid only. It should be noted that these ISD plots also contain a noise contribution as the curvature is a second derivative of the calculated interfaces.

Figure 2.g exhibits a distribution close to the $\kappa_1 = \kappa_2$ line, which is representative of the pore spherical shape. Figure 2.h and i feature a set of points aligned along a diagonal line ($\kappa_1 + \kappa_2 = cst$), in the area where the mean curvature of the pore is positive. Extracting the pressure difference ($p_p - p_l$) from the PhF results to calculate the mean curvature of the interface gives the black dotted line shown in figure 2.h and i. As can be seen, this line matches very well the measured principal curvature values. The fact that all the surface elements of the pore-liquid interface are along this line $(\kappa_1 + \kappa_2) = 2H$ ensures that the pressure within the pore is indeed uniform. The maximum density of these points in figure 2.h and i furthermore corresponds to the nearly spherical *tip* of the pore located in between 4 grains, close to the faces of the cubic RVE, for which $\kappa_1 = \kappa_2$. Besides, the points in the ISD plot also extend toward the line $\kappa_1 = 0$, i.e., $\kappa_2 = 2H$, which corresponds to the cylindrical-type shape of the pore located in between 2 grains (see figure 2.b and c). The extension towards this line is more pronounced for pore **c** which is spread over two octahedral sites. We can assume that a pore extended to various liquid channels, will exhibit a distribution further closer to $\kappa_1 = 0$ line, which is in fact in agreement with X-ray microtomography observations of Felberbaum et al [10], for Al-Cu specimens having a dendritic structure.

The predictions of the 2D and 3D model of Couturier [9] are also presented in figure 2.h and i. with a green square and circle, respectively. It can be observed that the 2D model of [9] does not provide a reasonable prediction of the pore curvature. However, their 3D model gives much better estimates. In this figure, the difference between their 3D model and the PhF results is very small compared to the situations reported in [12], because the corresponding pores have

been selected close to the maximum radius r_p^{max}, as already shown in figure 3.
Finally, in any case, the spherical tip of pores growing at high solid fraction will try to follow a path of maximum liquid space, i.e., minimal pore-liquid curvature. Even in a dendritic specimen, such spaces are found near the tips of the dendrites, and not near their roots. For example, in a specimen exhibiting a columnar structure, secondary dendrite arms tips are in a configuration close to that shown in figure 2. Therefore, the pinching model with $r_p^{mean} = (r_p^{max} + r_p^{min})/2$, might actually describe better the pinching effect in a dendritic specimen.

5. Conclusion

A 3D PhF model, which is capable of describing the complex morphology of pores growing in between a pre-existing solid phase, has been developed. The model accounts for segregation and diffusion of hydrogen, capillary forces at interfaces and the Laplace-Young's condition. The results show that the presence of the solid affects the pore morphology, which then influences its internal pressure, and thus its total volume.
The effect of globular grains on the pore morphology was studied and the PhF results were compared with the analytical model of Couturier et al. [9]. Based on the comparisons, and considering the fact that there is also a distribution of grain sizes in a real casting, we propose to use a radius r_p^{mean} for predicting the curvature overpressure in macroscopic porosity calculations.
In the present contribution, hydrogen diffusion in the solid is neglected due to its low solubility, but at high solid fraction, this cannot be neglected anymore [6]. On the other hand, although X-ray tomography characterization of as-solidified alloys has shed light on the curvature and complex morphology of pores, in-situ measurements during solidification should be made to further validate the present PhF results. Thanks to the advances in ultra-fast tomography techniques and the development of furnaces that can fit X-ray beam lines [16], this should be possible in the near future.

Acknowledgments

The authors would like to thank the Swiss Competence Centre for Materials Science and Technology (CCMX) and partner companies, Asulab, Constellium, Kugler Bimetal, Novelis, Rolex and Varinor, within the thematic area "Multi-scale, multi-phenomena modeling of metallic systems" for funding this research.

References

[1] Lee P D, Chirazi A and See D 2001 *Journal of Light Metals* **1** 15–30
[2] Niyama E, Uchida T, Morikawa M and Saito S 1982 *Int. Cast Met. J.* **7** 52–63
[3] Lee P D and Hunt J D 1997 *Acta Materialia* **45** 4155–4169
[4] Atwood R, Sridhar S, Zhang W and Lee P 2000 *Acta mater.* **48** 405 – 417
[5] Pequet C, Rappaz M and Gremaud M 2002 *Met. Trans.* **33 A** 2095–2106
[6] Carlson K D, Lin Z and Beckermann C 2007 *Metallurgical and Materials Transactions* **38 A** 541 – 555
[7] Poirier D, Yeum K and Maples A 1987 *Met. Trans.* **18 A** 1979–1987
[8] Kubo K and Pehlke R 1985 *Metallurgical and Materials Transactions B* **16** 359–366
[9] Couturier G and Rappaz M 2006 *Simulation of Aluminum Shape Casting Processing: From Alloy Design to Mechanical Properties* ed Wang Q, Krane M and Lee P (TMS Publ.) p 143
[10] Felberbaum M and Rappaz M 2011 *Acta Materialia* **59** 6849–6860
[11] Meidani H and Jacot A 2011 *Acta Materialia* **59** 3032–3040
[12] Meidani H, Desbiolles J L, Jacot A and Rappaz M 2012 *Acta Materialia* **(in press)**
[13] Boettinger W J, Warren J A, Beckermann C and Karma A 2003 *Annual Review of Materials Research* **32** 163–194
[14] Pressley A 2001 *Elementary Differential Geometry* (Springer-Verlag)
[15] Mendoza R, Alkemper J and Voorhees P 2003 *Metallurgical and Materials Transactions A* **34** 481–489
[16] Fife J, Rappaz M, Pistone M, Celcer T, Mikuljana C and Stampanoni M 2011 *J. Synchlotron Radiation* **(submitted)**